The Astrophysical Journal, 787:134 (12pp), 2014 June 1 doi:10.1088/0004-637X/787/2/134

ACTIVE GALACTIC NUCLEUS FEEDBACK IN THE HOT HALO OF NGC 4649

Alessandro Paggi[1], Giuseppina Fabbiano[1], Dong-Woo Kim[1], Silvia Pellegrini[2], Francesca Civano[3], Jay Strader[4], and Bin Luo[5]
[1] Harvard-Smithsonian Center for Astrophysics, 60 Garden Street, Cambridge, MA 02138, USA; apaggi@cfa.harvard.edu
[2] Department of Astronomy, University of Bologna, Via Ranzani 1, I-40127 Bologna, Italy
[3] Department of Physics and Yale Center for Astronomy and Astrophysics, Yale University, P.O. Box 208121, New Haven, CT 06520-8121, USA
[4] Department of Physics and Astronomy, Michigan State University, East Lansing, MI 48824, USA
[5] Department of Astronomy and Astrophysics, 525 Davey Laboratory, The Pennsylvania State University, University Park, PA 16802, USA
Received 2014 February 25; accepted 2014 April 16; published 2014 May 12

ABSTRACT

Using the deepest available *Chandra* observations of NGC 4649, we find strong evidences of cavities, ripples, and ring-like structures in the hot interstellar medium that appear to be morphologically related with the central radio emission. These structures show no significant temperature variations in correspondence with higher pressure regions (0.5 kpc $< r <$ 3 kpc). On the same spatial scale, a discrepancy between the mass profiles obtained from stellar dynamic and *Chandra* data represents the telltale evidence of a significant nonthermal pressure component in this hot gas, which is related to the radio jet and lobes. On a larger scale we find agreement between the mass profile obtained from *Chandra* data and planetary nebulae and globular cluster dynamics. The nucleus of NGC 4649 appears to be extremely radiatively inefficient, with highly sub-Bondi accretion flow. Consistent with this finding, the jet power evaluated from the observed X-ray cavities implies that a small fraction of the accretion power calculated for the Bondi mass accretion rate emerges as kinetic energy. Comparing the jet power to radio and nuclear X-ray luminosity, the observed cavities show behavior similar to those of other giant elliptical galaxies.

Key words: galaxies: individual (NGC 4649) – galaxies: ISM – ISM: jets and outflows – X-rays: galaxies – X-rays: ISM

Online-only material: color figures

1. INTRODUCTION

Evidence of the interaction of active galactic nuclei (AGNs) with the surrounding hot gas in nearby galaxies and clusters has been observed as morphological disturbances in the X-ray halos in the form of ripples and cavities (e.g., Fabian et al. 2000, 2003, 2006; Forman et al. 2005). The AGN-induced disturbances have also been observed in the hot interstellar medium (ISM) in the halos of a number of normal elliptical galaxies (e.g., Diehl & Statler 2007) and are interpreted as being a consequence of the thermal X-ray emitting gas being displaced by the AGN jets.

NGC 4649, also known as M60, is a nearby[6] X-ray-bright giant elliptical galaxy located in a group at the eastern edge of the Virgo Cluster. Its companion, located at ∼2.′5 to the northwest, is the spiral galaxy NGC 4647. NGC 4649 harbors a faint nuclear radio source (Condon et al. 2002). Although earlier *Chandra* data revealed a relaxed X-ray morphology close to hydrostatic equilibrium—first reported by Buote & Tsai (1995)— there has been a debate on the presence of inhomogeneities correlated with the nuclear radio source.

Finger-like structures in the inner ∼5 kpc of the diffuse X-ray emission from NGC 4649 have been reported by Randall et al. (2004, 2006) in their study of *Chandra* and *XMM-Newton* data. These structures are compared by the authors with those predicted by hydrodynamical simulations of cooling flows in elliptical galaxies (Kritsuk et al. 1998), that is, brighter, cooler inflowing gas surrounded by fainter, hotter outflowing jets. However, the authors found no significant temperature variations across the observed structures. Shurkin et al. (2008), using the same ∼37 ks *Chandra* observation of Randall et al. (2004) analysis, found morphological disturbances in the X-ray emitting gas and interpreted them as being the result of interaction with the central AGN. Instead, a subsequent analysis of deeper *Chandra* observations by Humphrey et al. (2008) showed a generally undisturbed X-ray morphology, consistent with that expected from a hot ISM in hydrostatic equilibrium. Later, the analysis by Dunn et al. (2010) of *Chandra* observations shallower than those of Humphrey et al.—but deeper than Shurkin et al.—revealed (again) disturbances and cavities in the ISM connected with the radio emission.

Due to the relatively small distance and large supermassive black hole (SMBH) mass (∼few $10^9\,M_\odot$) of NGC 4649, *Chandra* resolves radii close to the Bondi accretion radius, $r_{\rm acc} \approx$ 100–200 pc, at which the gravitational binding energy of a gas element becomes larger than its thermal energy (Bondi 1952). Thus, NGC 4649 represents an ideal case to investigate the following questions: what is the mass accretion rate? What fraction of the accretion power is in the observed nuclear luminosity, and what is in the observed jet power? Is NGC 4649 consistent with the previously found correlations between the Bondi mass accretion rate $\dot{M}_B$, the power associated with the observed cavities $P_{\rm cav}$, and radio luminosity (Cavagnolo et al. 2010; Russell et al. 2013)? Due to its low radio power and its not being a central dominant galaxy, NGC 4649 is also an ideal case to investigate whether these correlations, mostly found for radio-bright central dominant galaxies in groups or clusters, work equally well in more "normal" elliptical galaxies.

In this paper we revisit the properties of the hot ISM of NGC 4649, using much deeper *Chandra* data with respect to previous studies and updated atomic databases. We find strong evidence of cavities, ripples, and ring-like structures that appear to be morphologically related with the central radio emission. In addition, we find that the hot halo is subject to

[6] We assume a distance to NGC 4649 of 16 Mpc. At this distance 1″ corresponds to 77 pc.

Table 1
Observation Properties

Obs ID	Net Exposure (ks)	Date	PI Name
785	23.9	2000 Apr	Sarazin
8182	47.8	2007 Jan	Humphrey
8507	17.3	2007 Feb	Humphrey
12976	98.1	2011 Feb	Fabbiano
12975	79.8	2011 Aug	Fabbiano
14328	13.4	2011 Aug	Fabbiano

an additional nonthermal pressure term, as already reported in previous studies (e.g., Brighenti et al. 2009; Das et al. 2010, 2011; Humphrey et al. 2013). We show that the nonthermal pressure is found on the same spatial scale as the disturbances of the halo, and it is spatially correlated with the hot gas pressure and the minimum pressure derived from the radio data. The nucleus of NGC 4649 appears to be extremely radiatively inefficient, with highly sub-Bondi accretion flow, releasing a very small fraction of the accretion power in the form of kinetic energy in the surrounding halo.

The paper is organized as follows. Section 2 describes the data sets used in this work, the reduction procedures, and the image and spectral analysis. In Section 3 we discuss our results, and Section 4 is dedicated to our conclusions.

2. DATA REDUCTION AND ANALYSIS

NGC 4649 has been observed by *Chandra* with the ACIS detector (Garmire 1997) six times between 2000 April and 2011 August. Level 2 event data were retrieved from the *Chandra* Data Archive[7] and reduced with the CIAO (Fruscione et al. 2006) 4.5 software and the *Chandra* Calibration Data Base (CALDB) ver. 4.5.7, adopting standard procedures. After excluding time intervals of background flares exceeding 3σ with the LC_SIGMA_CLIP task, we obtained the low-background exposures listed in Table 1, for a total exposure of ∼280 ks.

For each data set we generated a full-resolution image in the 0.3–8.0 keV energy band. To take advantage of the longer exposure time and identify fainter signatures, we also produced a merged image of the six observations; to this end we used the WAVDETECT task to identify point sources in each observation with a two sequence of wavelet scales (i.e., 1, 2, 4, 8, 16, and 32 pixels) and a false-positive probability threshold of 10^{-6}. Then we used the REPROJECT_ASPECT task to modify the aspect solution minimizing position differences between the sources found and finally merged the images with the MERGE_ALL script.

2.1. Image of Halo

We examined the co-added image for evidence of morphological disturbances that may be connected with the nuclear radio source. To this end we then ran WAVDETECT on the merged image to detect fainter point sources. For each of these, appropriate elliptical regions were generated with the ROI CIAO task, both for the source and for the nearby background. We then processed the merged image with the DMFILTH task to remove the detected point sources, replacing the counts by sampling the Poisson distribution of the pixel values in the concentric background region. The resulting data image is therefore expected to show the morphology of the ISM diffuse emission, although it will still include point sources below the detection threshold.

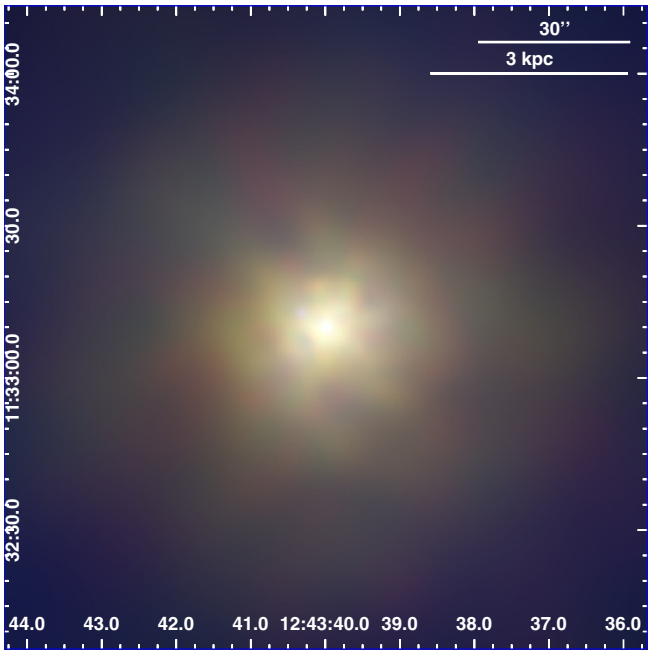

Figure 1. Merged three-color *Chandra* ACIS-S image of the inner ∼5 kpc region of NGC 4649. The three energy bands are shown with different colors, that is, 0.5–1.0 keV (red), 1.0–2.0 keV (green), and 2.0–8.0 keV (blue). Each band image is adaptively smoothed using the CSMOOTH tool. Besides some hard, nondetected (or not completely removed) point sources, the image shows hints of structures and cavities in the soft emission.

(A color version of this figure is available in the online journal.)

We produced separate images in different energy bands, (0.5–1.0 keV, 1.0–2.0 keV, and 2.0–8.0 keV), in order to obtain a three-color image that may pinpoint evidences of structures in the ISM. We then adaptively smoothed each band image using the CSMOOTH tool (Ebeling et al. 2006), with minimum and maximum significance signal-to-noise ratio (S/N) levels of 4.5 and 5.5, respectively, to enhance fainter, extended features of the diffuse emission. The merged three-color image (Figure 1) suggests hints of structures and cavities in the soft emission in the inner ∼3 kpc region.

To gain a more quantitative insight into morphological disturbances, we performed a one-dimensional fit of the surface brightness profile—evaluated in concentric annuli in the 0.3–8 keV source-free merged image—with a standard β model using SHERPA. The fit was performed in the inner 100″ (∼8 kpc) in order to avoid contamination from the emission of the companion galaxy NGC 4647. The results (Figure 2) show that, although the β model reproduces the large-scale behavior of the surface brightness profile, the fit is poor, with a reduced $\chi^2 \sim 4$. Adding a second β model did not increase the goodness of the fit, while yielding unphysical model parameters. Most of the χ^2 contribution comes from well-defined radii at ∼8″ and ∼40″ (corresponding to ∼0.5 kpc and 3 kpc, respectively).

To investigate the origin of these residuals, we performed a two-dimensional (2D) fit of the full-band source-free merged image with a 2D β model. Again, adding a second β model in our fit did not increase the fit goodness significantly. The residual distribution in the inner ∼1 kpc region is presented in the left panel of Figure 3, where we applied a 3 pixel FWHM Gaussian smoothing to highlight the presence of structures. In the same panel we superimpose onto the residual contours (shown in

[7] http://cda.harvard.edu/chaser

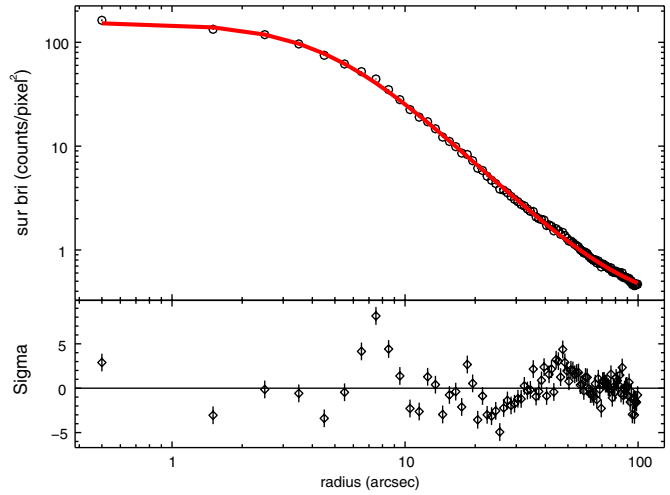

Figure 2. Radial profile of NGC 4649 0.3–8 keV surface brightness, with superimposed the best-fit β model fit. As discussed in the main text, the fit is very poor (with $\chi^2 \sim 4$) and shows significant residuals at $\sim 8''$ and $\sim 40''$.
(A color version of this figure is available in the online journal.)

green) the 1.4 GHz Very Large Array (VLA) emission contours (Stanger & Warwick 1986, shown in red). We notice a striking correlation between the outer radio lobes and the regions of negative residuals; regions of positive residuals appear to lie on both sides of the radio emission and are responsible for the features at a galactocentric radius of $\sim 8''$ seen in Figure 2. On a larger scale ($\sim 40''$), the residual map shows a ring-like structure—recalling those observed in NGC 1275 (e.g., Fabian et al. 2006)—as shown in Figure 4, where on the left panel we present the inner ~ 5 kpc region, where we applied a 10 pixel FWHM Gaussian smoothing. Radio emission contours are superimposed as in Figure 3. The significance of these structures is shown in the right panels of Figures 3 and 4. Here we show the residual S/N map, evaluated as the ratio between the residuals and the X-ray counts error, binned to a pixel size 4 and 14 times the size of the native ACIS-S pixel, respectively. At this pixel size the residual S/N map closely follows that of the residual map with the Gaussian smoothing, as shown by the superimposed contours of the residual map (shown in green). In particular, we notice that the S/N of the binned pixel in the observed structures is of the order of three or higher, pointing to a higher significance of the structures as a whole.

In order to evaluate the reliability of the observed structures and their dependence on the particular model used, we performed the 2D fitting procedure described above, excluding data between $5''$ and $70''$ (so avoiding the structures shown in Figure 4), and then subtracted the best-fit model so obtained from the complete data set. In addition, we repeated the same procedure in the four 90° quadrants to investigate possible azimuth anisotropies that could yield the observed structures. All of the residual maps so obtained are very similar and show the same structures presented in Figures 3 and 4. To investigate the effect of the point-source removal procedure described above on the observed residual structure, we also used the source catalog produced by Luo et al. (2013) (which used a finer $\sqrt{2}$ sequence of wavelet scales), obtaining again very similar results. We therefore conclude that the observed structures are real and do not strongly depend on the details of our analysis.

2.2. Spatially Resolved Spectral Analysis

To estimate the properties of the hot gas in the regions of enhanced and suppressed X-ray emission, we performed spectral analysis. Figure 5 shows the region used for spectral extraction with the CIAO SPECEXTRACT task. For each extraction region, background spectra were extracted in the same region from appropriate "blank-sky" fields and normalized equating

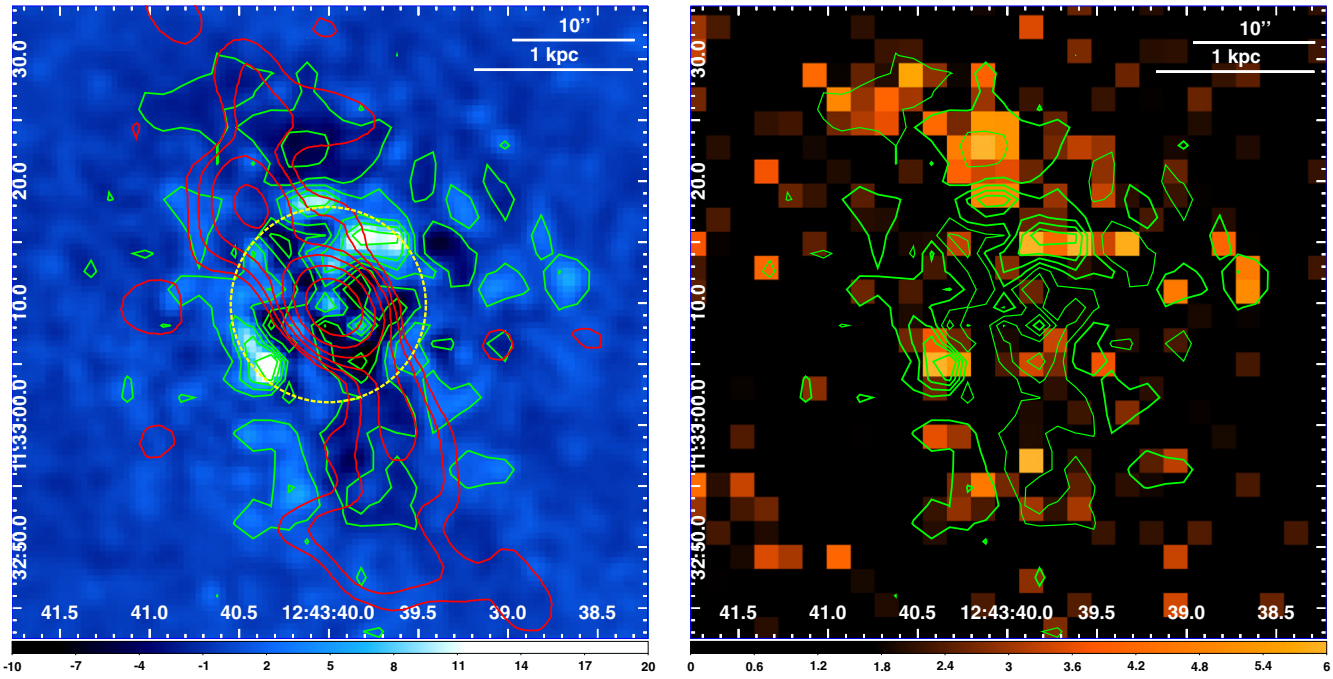

Figure 3. Left panel: distribution of residuals relative to an elliptical β model of the inner ~ 1 kpc region with a 3×3 FWHM Gaussian smoothing, with contours shown in green and VLA emission contours shown in red. The dashed yellow circle indicates the $\sim 8''$ radius where we see significant residuals in the one-dimensional surface brightness fit (see Figure 2). Right panel: residual S/N map, evaluated as the ratio between the residuals and the X-ray counts error, binned to a pixel size four times the size of the native ACIS-S pixel. Green contours are the same as in the left panel.
(A color version of this figure is available in the online journal.)

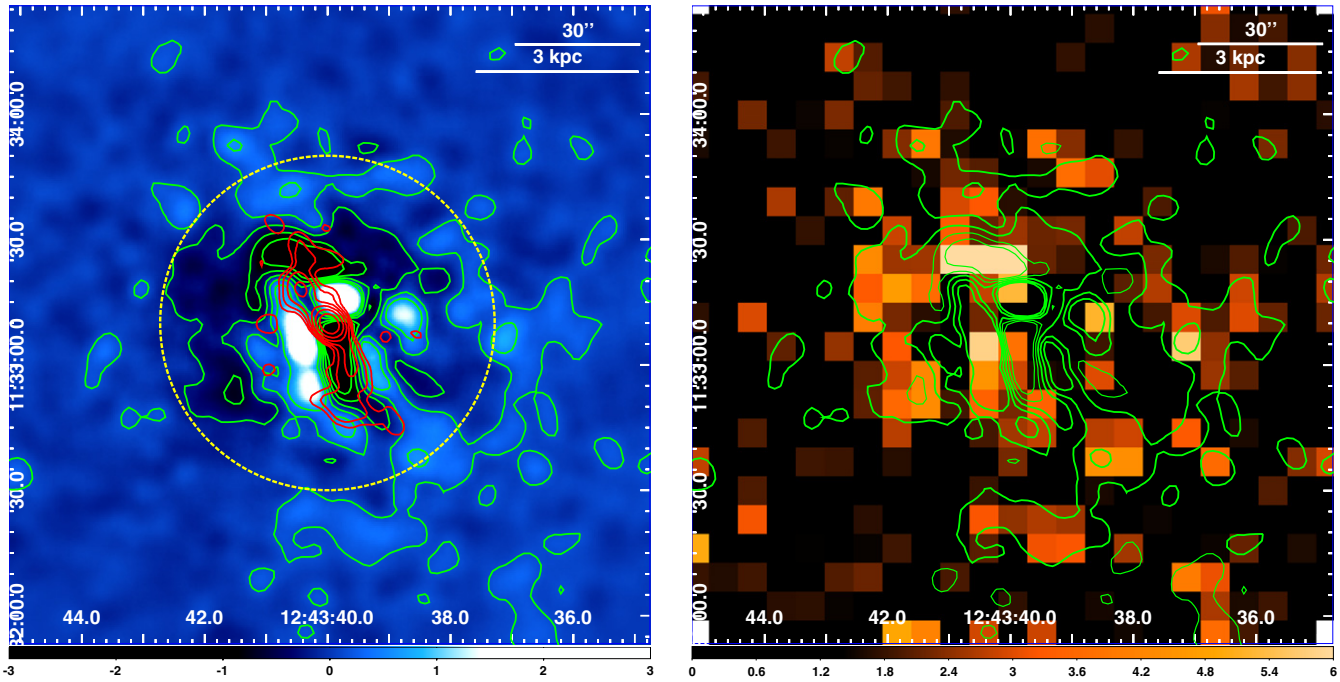

Figure 4. Same as Figure 3 but on a larger scale ∼5 kpc. Left panel: distribution of residuals relative to an elliptical β model, with a 10 × 10 FWHM Gaussian smoothing, with contours shown in green and VLA emission contours shown in red. The dashed yellow circle indicates the ∼40″ radius where we see significant residuals in the one-dimensional surface brightness fit (see Figure 2). Right panel: residual S/N map, evaluated as the ratio between the residuals and the X-ray counts error, binned to a pixel size 14 times the size of the native ACIS-S pixel. Green contours are the same as in the left panel.

(A color version of this figure is available in the online journal.)

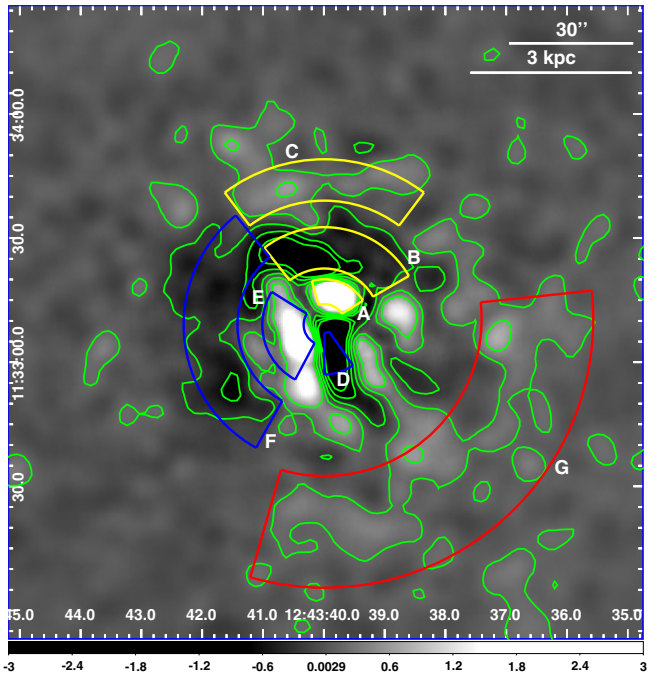

Figure 5. Same as in left panel of Figure 4 with superimposed the spectral extraction regions discussed in Section 2.2.

(A color version of this figure is available in the online journal.)

the 9–12 keV count rates of the observed and background data because essentially all of those hard X-rays are due to particle background (Hickox & Markevitch 2006). Additionally, we extracted spectra in a series of concentric, contiguous annuli, with widths chosen so as to contain approximately the same number of background-subtracted photons (∼12,000). We placed a lower limit of 2.″5 on the annulus width to ensure that the instrumental spatial resolution does not lead to strong mixing between the spectra in adjacent annuli. To account for projection effects, we used the PROJCT model implemented in XSPEC (version 12.8.0; Arnaud 1996). We excluded data in the vicinity of any detected point source and in the central part of the interloper galaxy NGC 4647 to prevent possible contamination. We extracted data individually for each observation and combined the source and background spectra, generating spectral response matrices weighted by the count distribution within the aperture (as appropriate for extended sources). To make use of the χ^2 fit statistic, we binned the spectra to obtain a minimum of 20 counts per bin using the SPECEXTRACT task; in the following, errors correspond to the 1σ confidence level for one interesting parameter ($\Delta\chi^2 = 1$). In all of the spectral fits we included photoelectric absorption by the Galactic column density along the line of sight $N_{\rm H} = 2.04 \times 10^{20}$ cm^{-2} (Kalberla et al. 2005).

Spectral fitting was performed in the 0.3–8 keV energy range using a model comprising a VAPEC thermal component plus a thermal bremsstrahlung component to account for undetected point sources (Irwin et al. 2003). We adopted solar abundances from Anders & Grevesse (1989), and we allowed the global ratios of O, Ne, Mg, and Si with respect to Fe to fit freely (see, e.g., Kim et al. 2012) and fixed the remaining ratios at the solar value. In addition, because NGC 4649 is within the Virgo Cluster, we included an additional hot gas component, with kT fixed at 2.5 keV (e.g., Gastaldello & Molendi 2002) to account for possible interloper cluster emission. The results are presented in Table 2. The details of the element abundances obtained in the fits will be discussed in a forthcoming paper (A. Paggi et al. 2014, in preparation). Here we concentrate on the physical parameters (temperature and gas density). In Figure 6 we show gas temperature and projected pressure $P_{\rm proj} = kT\ A^{1/2}$ (where A is the VAPEC component normalization per arcsec square) in

Table 2
Properties of the Spectra Extracted from the Regions Discussed in Section 2.2

Region	Net Counts (Error)	Residuals Sign.	χ^2 (dof)	kT (keV)	$P_{\rm proj}$ (10^{-4} keVcm$^{-5/2}$ arcsec^{-1})
A	7659 (88)	9	1.06 (90)	$0.86^{+0.02}_{-0.01}$	$7.17^{+0.55}_{-0.55}$
B	8454 (93)	11	1.03(99)	$0.86^{+0.01}_{-0.01}$	$3.22^{+0.27}_{-0.28}$
C	3865 (65)	6	1.00 (79)	$0.86^{+0.02}_{-0.01}$	$1.90^{+0.24}_{-0.25}$
D	5840 (77)	6	1.08 (76)	$0.85^{+0.01}_{-0.01}$	$5.92^{+0.54}_{-0.13}$
E	14565 (121)	7	1.08 (111)	$0.86^{+0.01}_{-0.01}$	$6.44^{+0.48}_{-0.48}$
F	8125 (93)	11	0.96 (102)	$0.87^{+0.01}_{-0.02}$	$1.94^{+0.18}_{-0.18}$
G	11657 (117)	10	1.07 (161)	$0.89^{+0.02}_{-0.02}$	$1.51^{+0.08}_{-0.08}$

Note. For each region we indicate its name, the net 0.3–8 keV counts, the residual significance in the region after subtracting the β model, and best-fit reduced χ^2, gas temperature and projected pressure with 1σ confidence errors.

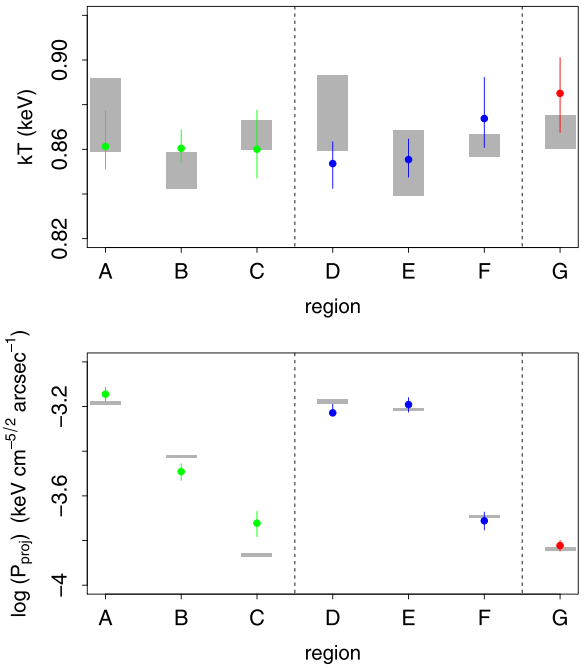

Figure 6. Spectral parameters from Table 2. The parameters are shown with colored points (according to the region colors shown in Figure 5) with errors reported in Table 2, whereas in gray we show the average values of the same parameters evaluated in concentric annuli at the same radius (see Section 2.2).
(A color version of this figure is available in the online journal.)

the extraction regions (shown in the corresponding colors) in comparison with the average values obtained in the annulus at the same radius (shown in gray). There is no significant temperature variation between overdense and underdense regions. Instead, the projected pressure is higher in brighter regions.

Figure 7 shows temperature and gas density profiles out to a radius of ∼20 kpc in comparison with that obtained with similar techniques by Humphrey et al. (2008) using shallower *Chandra* data. The temperature we derive is systematically higher than that of Humphrey et al. (2008), while our gas density is systematically lower. This effect is mainly due to the use of the updated ATOMDB 2.0.2 versus the 1.3.2 version available before 2010 (see Loewenstein & Davis 2012). In particular with respect to this previous analysis, while the gas density profiles have similar shapes, we see that our temperature profile, rather than exhibiting a decrease up to ∼1.5 kpc followed by a monotonic increase up to the outer regions, is characterized by a decrease up to ∼0.5 kpc followed by a "plateau" of almost constant temperature up to ∼3 kpc (the same scales of the structures shown in Figure 4). The two profiles are properly fitted by a double broken power-law model (shown in Figure 7 with the dashed lines), with breaks at ∼7.″6 (0.6 kpc) and ∼42.″2 (3.2 kpc).

3. DISCUSSION

In the local universe, most central SMBHs in elliptical galaxies are radiatively quiescent (Pellegrini 2005, 2010; Soria et al. 2006; Ho 2008; Gallo et al. 2010) and often seen in a "radio mode," where they are able to drive jets (e.g., Ho 2002; Merloni & Heinz 2007). Mechanical feedback of these jets has a significant impact on the surrounding ISM, with implications for galaxy and SMBH coevolution (e.g., Di Matteo et al. 2005; Croton et al. 2006; Sijacki et al. 2007; Ostriker et al. 2010; King 2013) and regulation of the hot gas cooling (Dunn et al. 2010). Many aspects of this feedback process, though, are not well understood, including the nature of the material feeding the SMBHs, the details of how accretion originates a mechanical energy output, in the form of a wind or a jet, and then how this couples to the surrounding ISM heating it. *Chandra* observations of hot gas-rich elliptical galaxies often show direct evidence of mechanical feedback in the form of radio jets and inflated bubbles displacing the hot plasma (e.g., McNamara & Nulsen 2007). From a study of nine X-ray luminous ellipticals harboring cavities, sufficiently nearby to measure the hot gas density and temperature reasonably close to the SMBH, a tight coupling was found between the Bondi mass accretion rate ($\dot{M}_B$) and the jet power estimated from the energy associated with the observed cavities $P_{\rm cav}$ (Allen et al. 2006; Merloni & Heinz 2007, see also Russell et al. 2013). The jet power $P_{\rm cav}$ correlates also with the (extended) radio luminosity, albeit in relationships showing a large scatter (Bîrzan et al. 2008; Cavagnolo et al. 2010; O'Sullivan et al. 2011).

Thanks to the long cumulative *Chandra* pointing on NGC 4649 we have determined the hot gas density and temperature in a wide range of radii, discovering cavities and a ring-like higher pressure ripple. We also determine these parameters in the nuclear region with unprecedented accuracy.

3.1. Temperature Profile

The residual map of the X-ray emission with respect to a standard β model (Figure 4) shows significant cavities and bright spots on a subkiloparsec scale as well as more extended ring-like structures at scales ∼3 kpc. These previously unreported features appear to be morphologically related with the weak

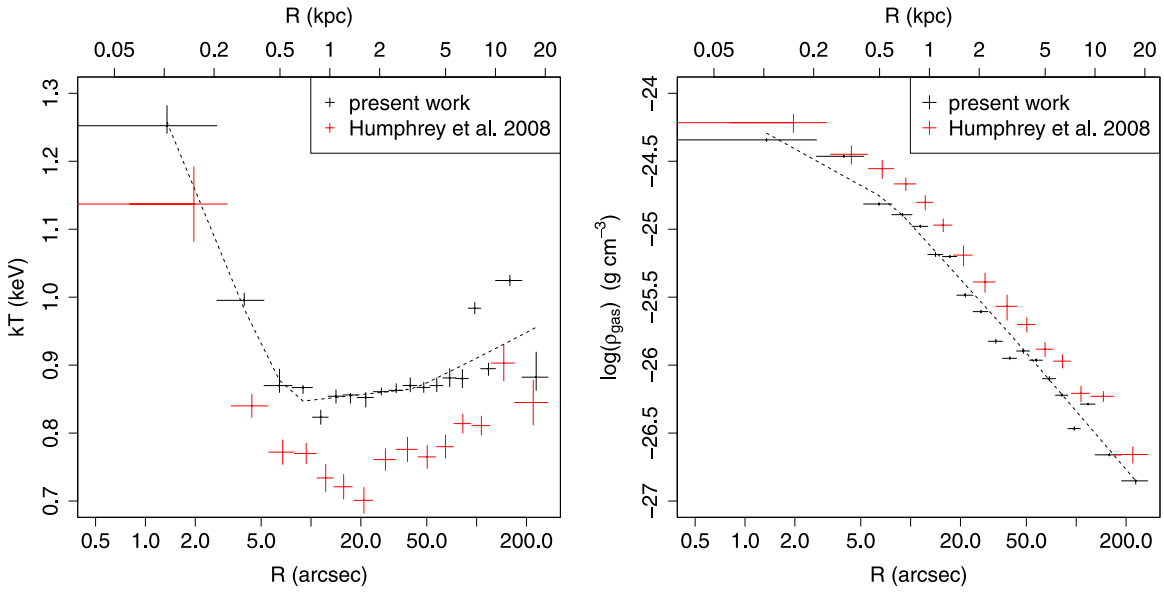

Figure 7. Gas temperature (left panel) and density (right panel) derived from the concentric annuli fit described in Section 2.2. Black crosses represent the profiles obtained in this work (error bars represent 1σ confidence level), whereas for comparison we show with red crosses the profiles obtained by (Humphrey et al. 2008) with shallower data (see Section 2.2).

(A color version of this figure is available in the online journal.)

nuclear radio source (Condon et al. 2002; Shurkin et al. 2008). We find no significant temperature variations between underdense and overdense regions (see Figure 6). Moreover, looking at the average temperature profile presented in Figure 7 (left panel), we see an almost constant temperature $\sim 0.85\,kT$ in the 0.5–3 kpc range. This resembles the case of the ripples and cavities around NGC 1275 in the Perseus cluster, discovered by Fabian et al. (2006) with *Chandra*, which also shows no sign of increased temperature in higher pressure regions. Fabian et al. concluded that the NGC 1275 structures may be isothermal waves whose energy is dissipated by viscosity, with thermal conduction and sound waves effectively distributing the energy from the radio source.

The radial kT profile of NGC 4649 shows a sudden increase up to $kT \sim 1.25$ keV in the inner 0.5 kpc. *Chandra* observations revealed central temperatures higher than the surroundings in other early-type galaxies with low or very low power radio sources: NGC 4594 (Pellegrini et al. 2003), NGC 4552 (Machacek et al. 2006), NGC 3115 (Wong et al. 2011), and NGC 4278 (Pellegrini et al. 2012). This hotter core has been interpreted as a result of heating from gravitational effects due to the central SMBH, a recent AGN outburst, or interaction with confined nuclear jets. The clear evidence for AGN feedback on the large scale in NGC 4649 (i.e., the series of cavities, likely more numerous than the N and S ones that will be investigated in detail in Section 3.5) provides support to the idea of repeated AGN heating occurring at the center, possibly producing the temperature peak, for example, through shock activity. Note that the radiative cooling time in the innermost radial bin is just $t_{\rm cool} \sim 2.9 \times 10^7$ yr (using the cooling curve from Sazonov et al. 2005); then if such cooling is to be offset, a heating mechanism is required. Following the calculation by Fabian et al. (2006), we can interpret the observed structures as isothermal waves and show that they can provide an effective way to heat the ISM. In fact, the thermal pressure deviations from the average value (shown in Figure 6) are about 5%–10% (comparable with those observed in NGC 1275, although with less significance). Then, such waves can balance radiative cooling if the cooling time is ~20 times the crossing time evaluated from the local sound speed ~500 km s^{-1} (Bîrzan et al. 2004). This condition is met because the cross time for the inner ~5 kpc region is $t_{\rm cross} \sim 1 \times 10^7$ yr, whereas the cooling time at this radius turns out to be $t_{\rm cool} \sim 5 \times 10^8$ yr. So, even if constraints on isothermal waves are not as tight as in the case of NGC 1275 due to larger uncertainties, it is possible for them to be the source of the ISM disturbances we observe in NGC 4649.

3.2. Nonthermal Pressure Component

To further investigate the origin of the observed ISM disturbances, we performed an analysis similar to that proposed by Humphrey et al. (2013), confronting the mass profiles obtained from the hot gas profiles presented in Figure 7 through the hydrostatic equilibrium equation and the ones obtained from independent diagnostics such as stellar kinematics, globular clusters (GCs), and planetary nebulae (PNe) velocities (Shen & Gebhardt 2010; Deason et al. 2012). The profiles are presented in Figure 8 (left panel); the hot gas-derived profile is in light blue and that from stellar and GC kinematics in red (Shen & Gebhardt 2010), with the width of the strips representing the relative uncertainties. In the outer regions the mass profiles from Deason et al. (2012) are plotted in green (GCs) and dark blue (PNe).

At larger radii we notice a significant discrepancy between the mass profile derived by Shen & Gebhardt (2010) using stellar (Gebhardt et al. 2003) and GC (Hwang et al. 2008) kinematics and the mass profiles obtained by Deason et al. (2012) using PNe (Teodorescu et al. 2011) and GC (same data set as Shen & Gebhardt) kinematics assuming spherical symmetry. We note that Deason et al. report that PNe are more centrally concentrated and are on more radial orbits with respect to the total GC population, whereas the red GC subpopulation is similar to that of both the stars and PNe. These discrepancies have been discussed by Teodorescu et al. (2011), Das et al. (2011), and Coccato et al. (2013), who suggested that GC and PNe may represent dynamically distinct systems. In addition, the analysis of stellar kinematics observation from the SLUGSS survey by

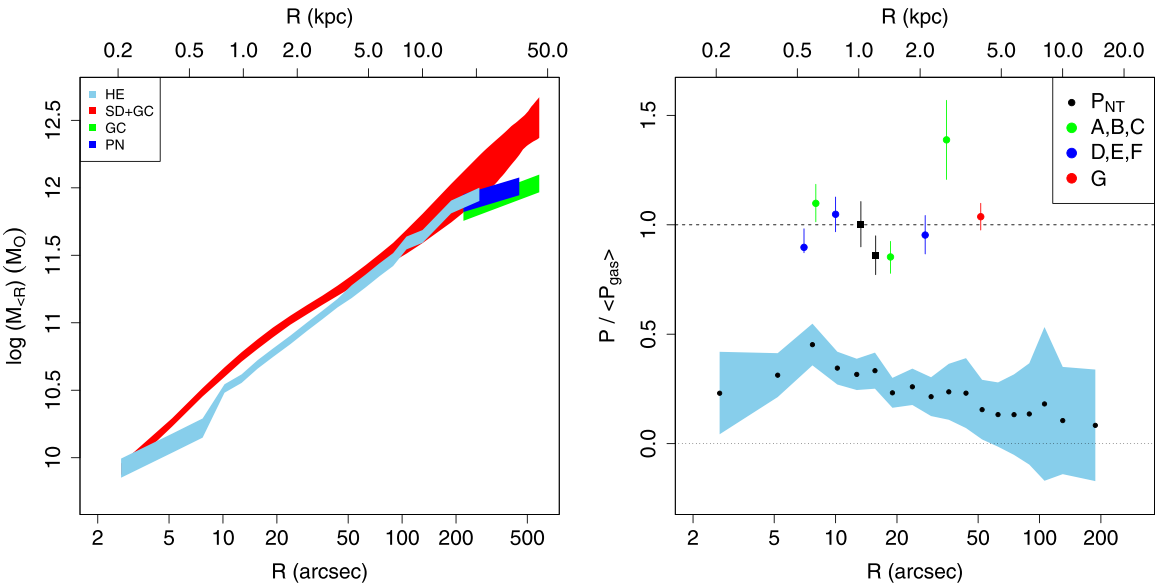

Figure 8. (Left panel: mass profiles obtained from the hydrostatic equilibrium Equation (1) (light blue strip) and from the stellar and GC kinematics by Shen & Gebhardt (2010, red strip). Note the significant deviation between 0.5 and 3 kpc. The mass profiles obtained by Deason et al. (2012) using PNe and GC kinematics are shown with a blue and green strip, respectively. Right panel: ratio of the nonthermal pressure component derived from Equation (3) to the average gas pressure (black circles, with the light blue strip representing the uncertainty). For comparison, we also present with colored points the ratio of the gas pressure in the regions shown in Figure 5, whereas the black squares represent the minimum radio pressure evaluated in Section 3.2.

(A color version of this figure is available in the online journal.)

Arnold et al. (2013) shows strong evidence for NGC 4649 of a fast-rotating embedded disk structure, pointing to this galaxy as a candidate for a major merger remnant. Finally, a recent analysis by D'Abrusco et al. (2014) revealed significant anisotropies in the two-dimensional distribution of GCs in NGC 4649, in particular in red and blue GC populations, that may affect these mass profiles. However, we note that the GC anisotropies revealed by D'Abrusco et al. (2014) are on a bigger scale than the ISM disturbances studied here.

In the inner radii, the mass profile from X-ray emitting hot gas and that from stellar and GC kinematics differ significantly between 0.5 and 3 kpc, again the same scales of the structures shown in Figure 4. In particular, the blue profile has been obtained using the equation

$$M_{\rm HE}(<R) = -R\,\frac{kT_g(R)}{G\mu m_p}\left(\frac{d\log\rho_g}{d\log R}+\frac{d\log T_g}{d\log R}\right), \quad (1)$$

where R is the radius, T_g is the gas temperature, ρ_g is the gas densities, m_p is the proton mass, and $\mu \approx 0.62$ is the average molecular weight factor. A nonthermal pressure term can, however, be added to Equation (1), that is

$$M(<R) = M_{\rm HE}(<R) - \frac{R^2}{G\,\rho_g(R)}\frac{dP_{\rm NT}}{dR}. \quad (2)$$

Assuming that the stellar kinematics profile accounts for the total mass expressed by Equation (2), we can estimate the nonthermal pressure term by writing

$$\frac{dP_{\rm NT}}{dR} = -\frac{G\,\rho_g(R)}{R^2}\left[M(<R) - M_{\rm HE}(<R)\right], \quad (3)$$

and $P_{\rm NT}$ can be obtained by numerically integrating Equation (3). In Figure 8 (right panel) we show the profile of the ratio between the nonthermal pressure and the average gas pressure obtained in the annular fit, which is consistent with that obtained by Humphrey et al. (2013). For comparison, in the same panel, we plot the ratio of gas pressure (i.e., excess and deficit in Figure 6(b)) in the same regions shown in Figure 5. Adopting the radio lobe parameters reported by Shurkin et al. (2008), we also computed the minimum radio pressure, assuming energy equipartition between particles and magnetic field in the jet (see, e.g., Hardcastle et al. 2004), and plotted it for N and S lobes in Figure 8 (right panel) as black squares. Although there are large uncertainties in these estimates, the radio jet pressure appears comparable with the thermal gas pressure at similar radii.

We note that the nonthermal pressure can account on average for ∼30% of the gas pressure in the regions of significant ISM disturbance and that there is a striking correlation between peaks and dips in the two pressure trends. A simple cross-correlation test between the two profiles yields that without any lag the correlation is significant at the ∼99%, indicating a correlation between the two profiles. This links the nonthermal pressure to the nuclear radio source and its jets. Humphrey et al. (2013) advanced several possibilities for the nonthermal pressure component observed in NGC 4649, including gas rotation, random turbulence, magnetic field, and cosmic-ray pressure. Our analysis strongly correlates the nonthermal pressure with the radio jet structure, and therefore we conclude that cosmic-ray injection into the ISM from the weak radio jets is the most likely origin of this pressure component.

3.3. Black Hole Mass Determination

To investigate the effects of the nonthermal pressure on the SMBH mass estimate, we fitted the mass profile derived with Equation (1) with the four standard galaxy mass components, that is, the gas component shown in Figure 7, the dark matter described by a standard Navarro–Frenk–White profile $\rho_{\rm DM} = \rho_0/[R/R_S(1+(R/R_S))^2]$, the stellar mass obtained from the observed V-band luminosity (Kormendy et al. 2009; with a free-to-vary M/L_V), and the central SMBH. The result of the fit

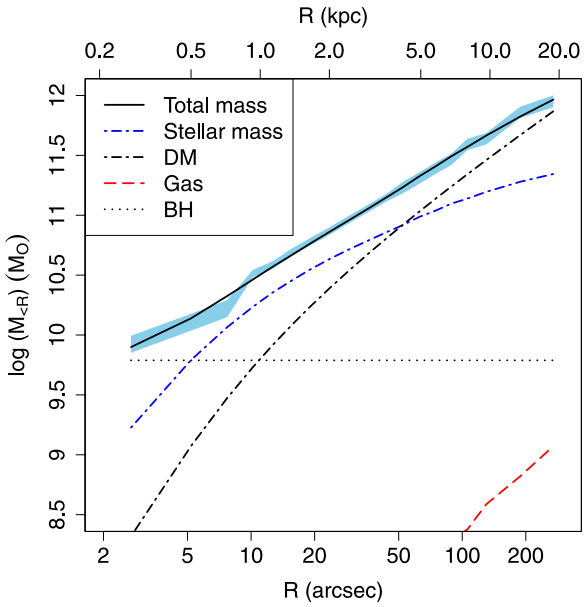

Figure 9. Fit of the mass profile derived with Equation (1) (blue strip) with the four standard galaxy mass components.

(A color version of this figure is available in the online journal.)

procedure is presented in Figure 9. The best-fit parameters are $\rho_0 = 9.6\,M_\odot$ kpc^{-3}, $R_S = 11.1$ kpc, and $M/L_V = 4.5$. These yield a SMBH mass estimate $M_{\rm BH} = (5.7 \pm 0.7) \times 10^9\,M_\odot$, compatible with—but nominally larger than—the SMBH mass estimate of $(4.5 \pm 1.0) \times 10^9\,M_\odot$ by Shen & Gebhardt (2010). Repeating the fitting procedure using the dark matter logarithmic profile proposed by Shen & Gebhardt (2010), we obtained a similar value of $M/L_V = 3.9$ but an even larger $M_{\rm BH} = (6.1 \pm 1.1) \times 10^9\,M_\odot$. Besides the details of the dark matter halo (more relevant in the outer regions), comparing with the mass profile from Shen & Gebhardt (2010), we note that the main effect of the nonthermal pressure (significant in the 0.5–3 kpc range) on this fitting procedure is to yield higher values of M/L_V, that is, a higher contribution of the stellar component to the total mass and as a consequence a lower SMBH mass. However, because the central SMBH mass is mainly driven by the mass profile in innermost radii, its estimate does not appear to be strongly affected by the presence of the nonthermal pressure component. We note, however, that our SMBH mass estimate is higher than the $(3.4 \pm 1.0) \times 10^9\,M_\odot$ value obtained by Humphrey et al. (2008) using shallower *Chandra* X-ray data. This discrepancy is explained with the higher gas temperature we observe with respect to Humphrey et al. (see Figure 7 and Equation (1)).

3.4. Nuclear Luminosity and Bondi Accretion

To evaluate the nuclear luminosity, we extracted the *Chandra*-ACIS spectrum of the inner $R = 2''$, adding to the model described in Section 2.2 a power-law component with photon index Γ fixed to two in order to model the AGN emission (e.g., Gallo et al. 2010). The nuclear luminosity within is therefore $L_{0.5-8\,\rm keV} = 7.2^{+1.3}_{-1.4} \times 10^{38}$ erg s^{-1}, $L_{0.3-10\,\rm keV} = 9.1^{+1.6}_{-1.7} \times 10^{38}$ erg s^{-1}, and $L_{2-10\,\rm keV} = 4.2^{+0.7}_{-0.8} \times 10^{38}$ erg s^{-1}. Given the mass of the SMBH, this X-ray nuclear emission corresponds to a very sub-Eddington bolometric emission. In fact, for a large sample of nearby low-luminosity AGNs, the median bolometric correction is $L_{\rm bol}/L_{2-10\,\rm keV} \approx 15.8$ (Ho 2008); Merloni & Heinz (2007) adopt $L_{\rm bol}/L_{2-10\,\rm keV} = 5$ for their study of 15 low-luminosity AGNs; Vasudevan & Fabian (2007) find $L_{\rm bol}/L_{2-10\,\rm keV} \approx 10$ for low-luminosity sources. The latter choice gives $L_{\rm bol,nuc} = 4.2 \times 10^{39}$ erg s^{-1}, and then $L_{\rm bol,nuc}/L_{\rm Edd} = 7.2 \times 10^{-9}$. From an estimate of the mass accretion rate $\dot{M}$, we can next discuss the accretion modalities.

The simplest assumption for gas accretion is that it is steady, spherically symmetric, with negligible angular momentum, as in the theory developed for gas accreting onto a point mass (Bondi 1952). The accretion rate $\dot{M}_B$ then comes from the gas density, temperature, and the SMBH mass, for which an accurate estimate is available for NGC 4649 ($4.5 \pm 1.0 \times 10^9\,M_\odot$; Shen & Gebhardt 2010). Ideally, one should insert in the $\dot{M}_B$ calculation the density and temperature at $r_{\rm acc} = 2GM_{\rm BH}/c_s(\infty)^2$, where the dynamics of the gas start to be dominated by the potential of the SMBH ($c_s(\infty)$ is the ambient sound speed; Frank et al. 2002). In practice, one uses fiducial temperature and density for the circumnuclear region, determined as close as possible to the SMBH. In our case, the gas properties are derived reasonably close to the black hole, thus giving a $\dot{M}_B$ estimate far better than usual (e.g., Pellegrini 2005; Russell et al. 2013). Inserting in $c_s(\infty)$ the temperature ($kT = 1.25^{+0.03}_{-0.01}$ keV) at the innermost bin, which extends out to 200 pc, gives $r_{\rm acc} = 121$ pc (for the polytropic index $\gamma = 5/3$ of the adiabatic case) or $r_{\rm acc} = 200$ pc ($\gamma = 1$, isothermal case). For the gas density of the innermost bin, $\rho_{\rm gas} = 4.54^{+0.12}_{-0.12} \times 10^{-25}$ g cm^{-3}, the Bondi mass accretion rate is $\dot{M}_B = 0.046\,M_\odot$ yr^{-1} for $\gamma = 5/3$ (as adopted hereafter; $\dot{M}_B$ would be 4.5 times larger if $\gamma = 1$; Frank et al. 2002). Taking into account the uncertainties on gas density, temperature, and SMBH mass and maximizing their effect on the computation of $\dot{M}_B$, the resulting range is $0.027 < \dot{M}_B(M_\odot\ {\rm yr}^{-1}) < 0.072$. The accretion power is then $P_B = 0.1\dot{M}_B c^2 = 2.6^{+1.5}_{-1.1} \times 10^{44}$ erg s^{-1}.

The nucleus of NGC 4649 is extremely radiatively inefficient, with $L_{\rm bol,nuc} \ll P_B$ (as already noticed Pellegrini 2005); our estimate of the accretion rate allows us to establish the accretion modalities. In fact $\dot{m}_B = \dot{M}_B/\dot{M}_{\rm Edd} = 4.6 \times 10^{-4}$, a very low value well within the radiatively inefficient accretion flow (RIAF) regime that can take place when $\dot{m} = \dot{M}/\dot{M}_{\rm Edd} \ll 0.01$ (Narayan & Yi 1995). The RIAF models are the viscous rotating analog of the spherical Bondi accretion, with an efficiency for producing radiation of $\epsilon \sim 10\dot{m}$. The expected $P_{\rm RIAF}$ is then $\sim 10\dot{m}_B\dot{M}_B c^2 = 1.2^{+1.8}_{-0.8} \times 10^{43}$ erg s^{-1}, that is $\sim$3000 times larger than $L_{\rm bol,nuc} = 4.2 \times 10^{39}$ erg s^{-1}. Adopting instead a bolometric correction factor specific for the spectral energy distribution of an RIAF, i.e., $L_{0.5-8\,\rm keV} \lesssim 0.15 L_{\rm bol,RIAF}$ (Mahadevan 1997), then $L_{\rm bol,RIAF} \gtrsim 4.8 \times 10^{39}$ erg s^{-1}, which is $\lesssim$2500 times lower than the predicted $P_{\rm RIAF}$. Reductions of the mass accretion rate with respect to the mass available at large radii (i.e., $\dot{M}_B$) on the way to the SMBH are possible because RIAF solutions include cases of outflows or convective motions (Blandford & Begelman 1999); another source of reduction is given by the possibility that the gas has nonnegligible angular momentum at the Bondi radius (Proga & Begelman 2003; Narayan & Fabian 2011). The latter authors calculated the rate at which mass accretes onto a SMBH from rotating gas, for plausible RIAF solutions for galactic nuclei, and found that $\dot{M} \sim (0.3\text{–}1)\dot{M}_B$. Indeed, the stellar component of NGC 4649 is known to possess a significant rotation (Pinkney et al. 2003). If $\dot{M} = 0.3\dot{M}_B$, the predicted $P_{\rm RIAF}$ goes down to $\sim 10^{42}$ erg s^{-1}, which is now larger than $L_{\rm bol,RIAF}$ by a factor between 100 and 600, considering the range for $\dot{M}_B$.

In conclusion, the accretion flow seems to emit less than predicted from the fuel observed to be available, even when allowing for an RIAF with angular momentum at the outer

Table 3
Power Estimates Evaluated in Sections 3.4 and 3.5

Name	Symbol	Value (erg s^{-1})	Note
Bondi luminosity	P_B	2.6×10^{44}	$P_B = 0.1\dot{M}_B c^2$
Bolometric luminosity	$L_{\rm bol,nuc}$	4.2×10^{39}	$L_{\rm bol}/L_{2-10\,\rm keV} = 10$
RIAF accretion power	$P_{\rm RIAF}$	1.2×10^{43}	$P_{\rm RIAF} = 10\dot{m}_B\dot{M}_B c^2$
RIAF accretion power + Ang. mom.	···	1.2×10^{42}	$\dot{M} = 0.3M_B$
RIAF bolometric luminosity	$L_{\rm bol,RIAF}$	4.8×10^{39}	$L_{\rm bol,RIAF}/L_{0.5-8\,\rm keV} \gtrsim 7$
Cavity power	$P_{\rm cav}$	3.8×10^{41}	Buoyancy rise
″	$P_{\rm cav}$	6.5×10^{41}	Sound-speed expansion

radius of the accretion flow (the various powers and luminosities considered here are summarized in Table 3); possible solutions could be that the bolometric correction is larger, so $L_{\rm bol,nuc}$ becomes larger (this is not expected to entirely fix the problem, though), or that the accretion flow should be modeled differently (i.e., with an even lower radiative efficiency), or that outflows/convective motions are important. We note that a very low radiation efficiency was also found in the deep ∼1 Ms *Chandra* observations of NGC 3115 (Wong et al. 2014; Shcherbakov et al. 2014), indicating for this source either a remarkably inefficient flow or a very low accretion rate suppressed by outflow, rotational support, or stellar feedback.

However, the total (observed) power output from the black hole is the sum of the radiating (e.g., $L_{\rm bol,nuc}$) and mechanical powers, where the latter by far usually dominates in the low-luminosity nuclei of the local universe. Therefore, a further important constraint on how much mass must be accreting comes from $P_{\rm cav}$ and is examined below.

3.5. Jet Power and Total Accretion Output

Pointed VLA observations by Shurkin et al. (2008) showed the radio properties at 1.4 GHz (see Figure 3) and their connection with the cavities in the hot ISM (from a shallower 37 ks *Chandra* exposure). Shurkin et al. derived a total flux density of 2.82×10^{-2} Jy at 1.4 GHz; for a distance of 16 Mpc, this gives a radio power of $P_{1.4} = 8.64 \times 10^{27}$ erg s^{-1} Hz^{-1}, that is $L_{1.4} = 1.2 \times 10^{37}$ erg s^{-1}. Thus NGC 4649 is a low-power radio source, one of the least radio emitting giant ellipticals with respect to those in the samples that produced the correlations between $\dot{M}_B$, $P_{\rm cav}$, and radio luminosity mentioned above; it is useful then to establish whether extrapolation to lower luminosity sources is applicable.

Following Allen et al. (2006), Shurkin et al. (2008) used the 1.4 GHz image to determine the edges of the cavities and then calculate the kinetic energy of the jet, as the sum of their internal energy and the PdV work done to inflate them (as $E = 4PV$). Because the majority of the energy carried off by these jets is mechanical, not radiative (e.g., Merloni & Heinz 2007), the resulting energy E, when divided by an approximate age for the cavities, gives an estimate of (a lower limit to[8]) the jet power $P_{\rm cav}$. When considering both age estimates for the cavities, based on the buoyancy rise-time and sound-speed expansion timescales, $P_{\rm cav}$ is in the range $(1–2) \times 10^{42}$ erg s^{-1}. This number is ∼0.003–0.009 of the accretion power P_B derived above.

We calculated the cavity power from our deeper image, adopting the same method as Shurkin et al., but rather than using the radio contours as a guide we used instead the X-ray residual map to delineate the cavities (see Figure 3). These are approximated as ellipsoids centered at distance R from the SMBH and with semi-axes r_l along the radio jet direction (31° east of north) and r_w across it (the semi-axis along the line of sight is taken equal to r_w). The regions shown in Figure 3 have $R = 18\farcs1$, $r_l = 7\farcs6$, $r_w = 10\farcs1$, and $R = 14\farcs1$, $r_l = 7\farcs5$, $r_w = 5\farcs2$ for the N and S cavities, respectively, with a 10% uncertainty on these sizes. We evaluated an energetic content $E_N = (1.9 \pm 0.8) \times 10^{55}$ erg and $E_S = (0.9 \pm 0.4) \times 10^{55}$ erg for the north and south cavity, respectively. The sound-speed expansion time has been evaluated as $t_{\rm cs} = r_l/c_s$, where $c_s = \sqrt{\gamma kT/\mu m_p}$ (Bîrzan et al. 2004), yielding $t_{\rm cs} = 1.37 \pm 0.14 \times 10^6$ yr and $1.36 \pm 0.14 \times 10^6$ yr for the N and S cavity, respectively. Buoyancy rise times are evaluated as $t_{\rm buoy} = R/v_{\rm buoy}$, where $v_{\rm buoy} \propto \sqrt{M(<R)\,r_l}/R$. Using $M(<R)$ from Equation (1), we obtain $t_{\rm buoy} = 2.66 \pm 0.41 \times 10^6$ yr and $1.85 \pm 0.28 \times 10^6$ yr for the N and S cavity, respectively.

We then obtained for the two N and S cavities, for the sound-speed expansion time $P_{\rm cav,N} = (4.47 \pm 1.88) \times 10^{41}$ erg s^{-1} and $P_{\rm cav,S} = (1.99 \pm 0.84) \times 10^{41}$ erg s^{-1}, and for the buoyancy rise time $P_{\rm cav,N} = (2.31 \pm 1.01) \times 10^{41}$ erg s^{-1} and $P_{\rm cav,S} = (1.46 \pm 0.65) \times 10^{41}$ erg s^{-1}. The two estimates are compatible between the errors and give a total $P_{\rm cav} \approx (3.8 \pm 1.2) \times 10^{41}$ erg s^{-1} (for the buoyancy rise time) and $P_{\rm cav} \approx (6.5 \pm 2.1) \times 10^{41}$ erg s^{-1} (for the sound-speed expansion time). Note that, as mentioned above, this may not be the whole of the mechanical power injected in the hot ISM; shocks are not seen here, but possibly sound waves are. Moreover, in addition to the larger cavities close to the ends of the jets, there are other smaller cavities seen in the X-ray gas (as well as other smaller radio structures; see Figure 2 of Shurkin et al.). The total of $P_{\rm cav}$ is then such that $P_{\rm cav}/P_B \gtrsim 0.0025$.

In the correlation found by Allen et al. (2006) between $P_{\rm cav}$ and P_B for a sample of elliptical galaxies, on average $P_{\rm cav} \approx 0.2\,P_B$, a much larger fraction than found here. For NGC 4649, which has P_B equal to the largest one in the Allen et al. sample, a larger $P_{\rm cav}$ is predicted from our P_B by their correlation: $P_{\rm cav} = 9.9 \times 10^{43}$ erg s^{-1} (with $P_{\rm cav} = 3.8 \times 10^{43}$ erg s^{-1} the lowest value allowed by all of the uncertainties on $\dot{M}_B$ and on the correlation coefficients), about 100 times larger than the jet power we estimate above. Allen et al.'s relation implies that a significant fraction of P_B emerges as kinetic energy, which requires that a significant fraction of the mass entering $r_{\rm acc}$ flows all the way down to the SMBH, with little mass loss (in outflows) along the way. This seems not to be the case here, consistent with the results of the previous section, where a significant reduction of $\dot{M}$ with respect to $\dot{M}_B$ was needed. A similar result is obtained if one were to infer the accretion rate from the "observed" $L_{\rm nuc,bol} = 4.2 \times 10^{39}$ erg s^{-1}. For the RIAF low

[8] Shocks and sound waves have also been found to contribute significantly to the power output of the central AGN (e.g., Fabian et al. 2006; Forman et al. 2007; Randall et al. 2011).

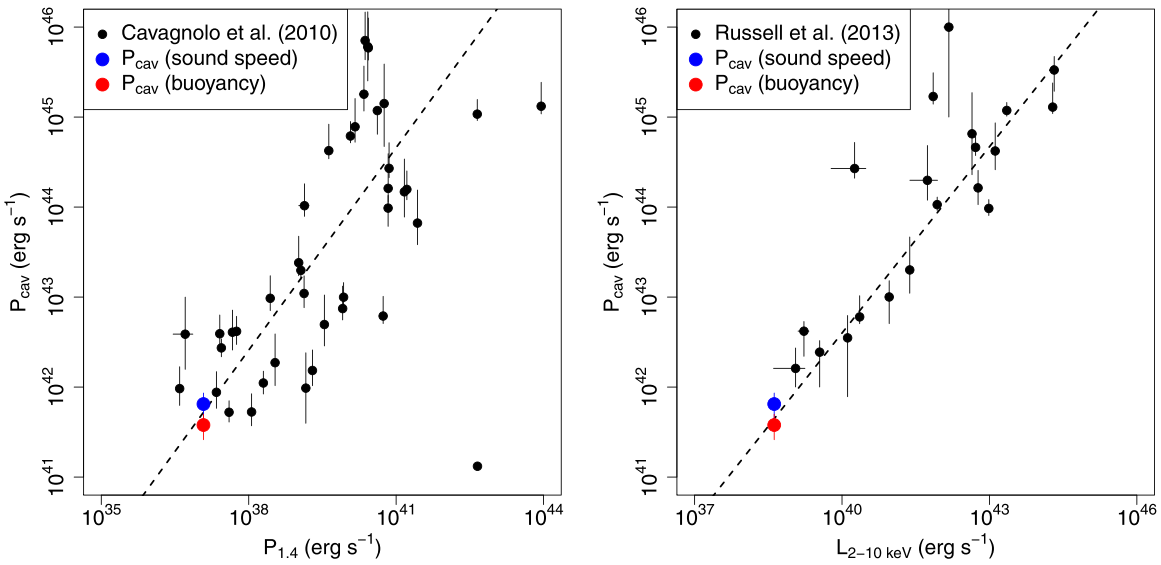

Figure 10. Left panel: cavity power vs. radio power in the sample of giant elliptical galaxies from Cavagnolo et al. (2010; black circles) and in NGC 4649 evaluated from the sound-speed expansion time (blue circle) and from the buoyancy rise time (red circle). The dashed line represents the best-fit relation from Cavagnolo et al. Right panel: cavity power vs. nuclear X-ray luminosity in the sample of bright galaxy cluster from Russell et al. (2013; black circles) and in NGC 4649 (same as in left panel). The dashed line represents the best-fit relation from Russell et al.

(A color version of this figure is available in the online journal.)

radiative efficiency, one would derive $\dot{M} = 8.5 \times 10^{-4}\ M_{\odot}\ \mathrm{yr}^{-1}$, that is $\dot{M} \sim 0.02\ \dot{M}_B$. Such a value for $\dot{M}$ gives $P \approx 0.1\ \dot{M}c^2 = 4.9 \times 10^{42}$ erg s^{-1}, which can still account for the measured $P_{\rm cav}$ (and is much closer to it, $P_{\rm cav}/P \sim 0.1$). So, it seems that the same reduction in $\dot{M}$ required by the (far smaller) nuclear luminosity could explainal so the (far larger) accretion output observed in mechanical form. We note that Russell et al. (2013) were not able to reproduce Allen et al.'s relation. This is mainly due to a different method for delineating the cavities adopted in the two papers, that is, radio maps for Allen et al. and X-ray maps for Russell et al. (the same method adopted in the present paper). As a result, the trend between cavity power and Bondi power appears significantly weakened in Russell et al.'s analysis (see their Figure 11) and with a larger scatter due to the different profiles adopted by these authors to extrapolate the gas density profiles to the accretion radius. In addition we note that in principle $P_{\rm cav}$ is an average over the $\sim$1.4–2.7 $\times$ 10^6 yr age of the cavities, whereas $L_{\rm bol,nuc}$ is a measurement of the instantaneous accretion rate (because the flow time from $r_{\rm acc}$ to the SMBH is very small, of the order of $\sim 2 \times 10^5$ yr). Thus when linking $\dot{M}$ to $P_{\rm cav}$ we assume that the accretion flow has been the same over the past $\sim$ few 10^6 yr.

Note that NGC 4649 does not display extended optical emission line regions and is depleted of molecular and atomic gas, as shown by Young (2002), which put an upper limit of $6.8 \times 10^7\ M_{\odot}$ to the H_2 mass content of this galaxy. If we assume that the AGN mechanical power we evaluate in the cavities is generated by accretion at $\sim 0.1 \dot{M}c^2$, the total accreted mass to power the jet would be $\sim$300 $M_{\odot}$, well below the upper limit evaluated by Young. However, in NGC 4649 there is (as in general for hot gas-rich galaxies) a large hot gas reservoir $\sim 3 \times 10^9\ M_{\odot}$, much larger than the cold gas upper limit. Then, on a secular scale it is more likely that accretion is taking and took place thanks to the hot gas. Even if the primary source of accretion is likely to be the hot gas, however, the low accretion rate we evaluate does not exclude molecular gas as a source of fuel for the SMBH, so cold accretion of molecular and atomic gas represents a possible alternate (or additional) scenario to Bondi accretion.

3.6. Jet Power, Radio, and Nuclear Luminosity

Cavagnolo et al. (2010) re-examined the scaling relationship between jet power, $P_{\rm jet}$, and synchrotron luminosity at 1.4 GHz and 200–400 MHz, incorporating measurements for 21 giant elliptical galaxies, thus expanding the sample of Bîrzan et al. (2008), dominated by bubbles in clusters, to lower radio power sources. The $P_{\rm jet}$ was estimated as $P_{\rm cav}$, the power required to inflate the cavities. The Cavagnolo et al. relationship predicts $P_{\rm cav} = 5.2 \times 10^{41}$ erg s^{-1} from $L_{1.4}$ of NGC 4649 and between 8.7×10^{40} and 3.2×10^{42} erg s^{-1}, considering the large scatter around the correlation[9] of 0.78 dex. This range of $P_{\rm cav}$ includes the direct estimate from Section 3.5 (see Figure 10, left panel). Similar results are obtained for the O'Sullivan et al. (2011) $P_{\rm cav}$–$L_{1.4}$ relation. Thus, NGC 4649 seem to host cavities similar in nature to those of other giant ellipticals, at least for their radio properties, i.e., the relation between radiative and mechanical energy of the jets.

The nuclear 2–10 keV luminosity of NGC 4649 also fits on the correlation between nuclear 2–10 keV luminosity and $P_{\rm cav}$, derived for 27 detected nuclei of central dominant galaxies (Russell et al. 2013; see also Merloni & Heinz 2007). The majority of the sample is in an RIAF mode, and the mechanical cavity power dominates the radiative output. NGC 4649 sits

[9] The $P_{\rm cav}$–$P_{1.4}$ relation shows a large scatter, possibly due to the fact that the radio emission from lobes depends on their composition and processes such as gas entrainment, shocks, and aging. In the case of NGC 4649 we do not see evidence of shocks. Shurkin et al. investigated the particle content of the cavities by determining k/f, where k is the ratio of the total particle energy contained in the cavity to the energy accounted for by electrons emitting synchrotron radiation in the range of 10 MHz to 10 GHz, and f is the volume filling factor of the relativistic plasma in the cavity. In general, k/f is in the range of $\sim$1–1000 for cavities that are active, whereas the values for NGC 4649 are very large ($\sim 10^4$). This could be explained by entrained particles or electrons that have aged, which is likely given the small radio flux; NGC 4649 could soon become a ghost cavity system.

at the lowest values of the correlation, with $L_{2-10\,\mathrm{keV}} = 4.2 \times 10^{38}$ erg s^{-1}, from which we can predict $P_{\mathrm{cav}} \sim 4 \times 10^{41}$ erg s^{-1} (see Figure 10, right panel). Even though also in this correlation the scatter is large, it was taken as evidence that the radiative efficiency of the X-ray nucleus increases with increasing P_{cav} until the quasar regime is reached (where the nuclear luminosity becomes comparable to P_{cav}).

4. SUMMARY AND CONCLUSIONS

We investigated the presence of AGN feedback in the ISM of the giant elliptical NGC 4649 by using a total of 280 ks *Chandra* observations. This source has been studied several times in different wavelengths and in particular in the X-rays (e.g., Churazov et al. 2010; Das et al. 2010; Loewenstein & Davis 2012). Shurkin et al. (2008) and Humphrey et al. (2008), making use of *Chandra* observations, studied the properties of the ISM in NGC 4649 using the unsharp-mask technique, looking for morphological disturbances pointing to deviations from the hydrostatic equilibrium condition suggested by the generally relaxed X-ray morphology. Interestingly, whereas the former authors using a shallow ∼37 ks observation found evidences of structures and cavities in the ISM that they interpreted as connected with the central, faint radio source, the latter authors using deeper ∼81 ks data did not find any evidence of such disturbances. A subsequent analysis by Dunn et al. (2010) showed disturbances and cavities in the ISM as residuals of the X-ray surface brightness from a spherical β model, connected with the radio emission.

Using much deeper *Chandra* data with a total exposure ∼280 ks, we used the latter approach to investigate the morphological distribution of the ISM in NGC 4649. We studied the deviation of the X-ray surface brightness from an elliptical β model, which is expected to describe the hot gas distribution in relaxed galaxies. The residuals of this fitting procedure, presented in Figure 4, show significant cavities, ripples, and ring-like structures on the inner 0.5–3 kpc scale. This is at variance with the $\lesssim 2\sigma$ significance of the cavities reported by Shurkin et al. (2008) as evaluated by Humphrey et al. (2008). The deeper data considered here revealed these structures with high significance; moreover, the structures appear to be morphologically related with the central radio emission, with cavities lying in correspondence with the extended radio lobes and regions of enhanced emission situated on the side of them and, on a larger scale, taking the form of ring-like ripples, which seems reminiscent of the structures observed in NGC 1275 (Fabian et al. 2006). In common with this source, we found no significant temperature variations in correspondence with higher pressure regions. So, if radio ejecta driven shocks are responsible for the observed ISM morphology, the observed structures may be isothermal waves whose energy is dissipated by viscosity, with thermal conduction and sound waves effectively distributing the energy from the radio source. Evidences of deviations from the hydrostatic equilibrium are also provided by the mass profiles presented in Figure 8 (left panel). A significant nonthermal pressure is found on the same scale as the residual structures, where it reaches ∼30% of the observed gas pressure. In addition, the excess gas pressure and nonthermal pressure profiles appear to be strongly correlated, indicating the radio ejecta as the likely origin for this additional pressure component.

At smaller scales, similarly to a few other early-type galaxies harboring low-power radio sources, NGC 4649 shows increased temperatures in the inner 0.5 kpc region. The nucleus of NGC 4649 appears to be extremely sub-Eddington, with the accretion flow emitting less than predicted from the fuel observed to be available, even when allowing for an RIAF with angular momentum at the outer radius of the accretion flow. Also, the jet power evaluated from the observed X-ray cavities appears to be much smaller than that predicted for elliptical galaxies from the Bondi accretion power P_B. If the mass accretion rate accounting for the observed nuclear X-ray luminosity is adopted—which requires, in addition to a low radiative efficiency, a significant reduction of the accretion rate with respect to the Bondi value, due, e.g., to outflows/convective motions—then the corresponding accretion power P is ∼10 times larger than the observed kinetic power. When comparing the jet power to radio and nuclear X-ray luminosity, on the other hand, the observed cavities show behavior similar to those of other giant elliptical galaxies.

We acknowledge useful comments and suggestions by our anonymous referee. This work was partially supported by NASA contract NAS8-03060 (*CXC*), and NASA *Chandra* grant G01-12110X. D.W.K. acknowledges partial support from Smithsonian Institute 2014 Competitive Grants Program for Science. S.P. acknowledges financial support from MIUR grant PRIN 2010–2011, project "The Chemical and Dynamical Evolution of the Milky Way and Local Group Galaxies," prot. 2010LY5N2T. F.C. acknowledges financial support by the NASA contract 11-ADAP11-0218. This research has made use of software provided by the *Chandra X-ray Center* (*CXC*) in the application packages CIAO, ChIPS, and Sherpa.

REFERENCES

Allen, S. W., Dunn, R. J. H., Fabian, A. C., Taylor, G. B., & Reynolds, C. S. 2006, MNRAS, 372, 21
Anders, E., & Grevesse, N. 1989, GeCoA, 53, 197
Arnaud, K. A. 1996, in ASP Conf. Ser. 101, Astronomical Data Analysis Software and Systems V, ed. G. H. Jacoby & J. Barnes (San Francisco, CA: ASP), 17
Arnold, J. A., Romanowsky, A. J., Brodie, J. P., et al. 2013, arXiv:1310.2607
Bîrzan, L., McNamara, B. R., Nulsen, P. E. J., Carilli, C. L., & Wise, M. W. 2008, ApJ, 686, 859
Bîrzan, L., Rafferty, D. A., McNamara, B. R., Wise, M. W., & Nulsen, P. E. J. 2004, ApJ, 607, 800
Blandford, R. D., & Begelman, M. C. 1999, MNRAS, 303, L1
Bondi, H. 1952, MNRAS, 112, 195
Brighenti, F., Mathews, W. G., Humphrey, P. J., & Buote, D. A. 2009, ApJ, 705, 1672
Buote, D. A., & Tsai, J. C. 1995, ApJ, 452, 522
Cavagnolo, K. W., McNamara, B. R., Nulsen, P. E. J., et al. 2010, ApJ, 720, 1066
Churazov, E., Tremaine, S., Forman, W., et al. 2010, MNRAS, 404, 1165
Coccato, L., Arnaboldi, M., & Gerhard, O. 2013, MNRAS, 436, 1322
Condon, J. J., Cotton, W. D., & Broderick, J. J. 2002, AJ, 124, 675
Croton, D. J., Springel, V., White, S. D. M., et al. 2006, MNRAS, 365, 11
D'Abrusco, R., Fabbiano, G., Mineo, S., et al. 2014, ApJ, 783, 18
Das, P., Gerhard, O., Churazov, E., & Zhuravleva, I. 2010, MNRAS, 409, 1362
Das, P., Gerhard, O., Mendez, R. H., Teodorescu, A. M., & de Lorenzi, F. 2011, MNRAS, 415, 1244
Deason, A. J., Belokurov, V., Evans, N. W., & McCarthy, I. G. 2012, ApJ, 748, 2
Diehl, S., & Statler, T. S. 2007, ApJ, 668, 150
Di Matteo, T., Springel, V., & Hernquist, L. 2005, Natur, 433, 604
Dunn, R. J. H., Allen, S. W., Taylor, G. B., et al. 2010, MNRAS, 404, 180
Ebeling, H., White, D. A., & Rangarajan, F. V. N. 2006, MNRAS, 368, 65
Fabian, A. C., Sanders, J. S., Allen, S. W., et al. 2003, MNRAS, 344, L43
Fabian, A. C., Sanders, J. S., Ettori, S., et al. 2000, MNRAS, 318, L65
Fabian, A. C., Sanders, J. S., Taylor, G. B., et al. 2006, MNRAS, 366, 417
Forman, W., Jones, C., Churazov, E., et al. 2007, ApJ, 665, 1057
Forman, W., Nulsen, P., Heinz, S., et al. 2005, ApJ, 635, 894
Frank, J., King, A., & Raine, D. J. (ed.) 2002, in Accretion Power in Astrophysics (Cambridge: Cambridge Univ. Press), 398

Fruscione, A., McDowell, J. C., Allen, G. E., et al. 2006, Proc. SPIE, 6270, 62701
Gallo, E., Treu, T., Marshall, P. J., et al. 2010, ApJ, 714, 25
Garmire, G. P. 1997, BAAS, 29, 823
Gastaldello, F., & Molendi, S. 2002, ApJ, 572, 160
Gebhardt, K., Richstone, D., Tremaine, S., et al. 2003, ApJ, 583, 92
Hardcastle, M. J., Harris, D. E., Worrall, D. M., & Birkinshaw, M. 2004, ApJ, 612, 729
Hickox, R. C., & Markevitch, M. 2006, ApJ, 645, 95
Ho, L. C. 2002, ApJ, 564, 120
Ho, L. C. 2008, ARA&A, 46, 475
Humphrey, P. J., Buote, D. A., Brighenti, F., Gebhardt, K., & Mathews, W. G. 2008, ApJ, 683, 161
Humphrey, P. J., Buote, D. A., Brighenti, F., Gebhardt, K., & Mathews, W. G. 2013, MNRAS, 430, 1516
Hwang, H. S., Lee, M. G., Park, H. S., et al. 2008, ApJ, 674, 869
Irwin, J. A., Athey, A. E., & Bregman, J. N. 2003, ApJ, 587, 356
Kalberla, P. M. W., Burton, W. B., Hartmann, D., et al. 2005, A&A, 440, 775
Kim, D.-W., Fabbiano, G., & Pipino, A. 2012, ApJ, 751, 38
King, A. 2013, SSRv, 85
Kormendy, J., Fisher, D. B., Cornell, M. E., & Bender, R. 2009, ApJS, 182, 216
Kritsuk, A., Bohringer, H., & Muller, E. 1998, MNRAS, 301, 343
Loewenstein, M., & Davis, D. S. 2012, ApJ, 757, 121
Luo, B., Fabbiano, G., Strader, J., et al. 2013, ApJS, 204, 14
Machacek, M., Nulsen, P. E. J., Jones, C., & Forman, W. R. 2006, ApJ, 648, 947
Mahadevan, R. 1997, ApJ, 477, 585
McNamara, B. R., & Nulsen, P. E. J. 2007, ARA&A, 45, 117
Merloni, A., & Heinz, S. 2007, MNRAS, 381, 589
Narayan, R., & Fabian, A. C. 2011, MNRAS, 415, 3721
Narayan, R., & Yi, I. 1995, ApJ, 452, 710
Ostriker, J. P., Choi, E., Ciotti, L., Novak, G. S., & Proga, D. 2010, ApJ, 722, 642
O'Sullivan, E., Giacintucci, S., David, L. P., et al. 2011, ApJ, 735, 11
Pellegrini, S. 2005, ApJ, 624, 155
Pellegrini, S. 2010, ApJ, 717, 640
Pellegrini, S., Baldi, A., Fabbiano, G., & Kim, D.-W. 2003, ApJ, 597, 175
Pellegrini, S., Wang, J., Fabbiano, G., et al. 2012, ApJ, 758, 94
Pinkney, J., Gebhardt, K., Bender, R., et al. 2003, ApJ, 596, 903
Proga, D., & Begelman, M. C. 2003, ApJ, 592, 767
Randall, S. W., Forman, W. R., Giacintucci, S., et al. 2011, ApJ, 726, 86
Randall, S. W., Sarazin, C. L., & Irwin, J. A. 2004, ApJ, 600, 729
Randall, S. W., Sarazin, C. L., & Irwin, J. A. 2006, ApJ, 636, 200
Russell, H. R., McNamara, B. R., Edge, A. C., et al. 2013, MNRAS, 432, 530
Sazonov, S. Y., Ostriker, J. P., Ciotti, L., & Sunyaev, R. A. 2005, MNRAS, 358, 168
Shcherbakov, R. V., Wong, K.-W., Irwin, J. A., & Reynolds, C. S. 2014, ApJ, 782, 103
Shen, J., & Gebhardt, K. 2010, ApJ, 711, 484
Shurkin, K., Dunn, R. J. H., Gentile, G., Taylor, G. B., & Allen, S. W. 2008, MNRAS, 383, 923
Sijacki, D., Springel, V., Di Matteo, T., & Hernquist, L. 2007, MNRAS, 380, 877
Soria, R., Fabbiano, G., Graham, A. W., et al. 2006, ApJ, 640, 126
Stanger, V. J., & Warwick, R. S. 1986, MNRAS, 220, 363
Teodorescu, A. M., Méndez, R. H., Bernardi, F., et al. 2011, ApJ, 736, 65
Vasudevan, R. V., & Fabian, A. C. 2007, MNRAS, 381, 1235
Wong, K.-W., Irwin, J. A., Shcherbakov, R. V., et al. 2014, ApJ, 780, 9
Wong, K.-W., Irwin, J. A., Yukita, M., et al. 2011, ApJL, 736, L23
Young, L. M. 2002, AJ, 124, 788